Nano Research

Open Access

Research Article

Janus MXene film with gradient structure for highly efficient terahertz and infrared electromagnetic absorption

Shaodian Yang[1,2], Weiqiang Huang[1], Zhiqiang Lin[2], Zibo Chen[1], Rongliang Yang[1], Yi Jia[3], Xuebin Liu[1], Rui Wang[1,4], Zhiping Zeng[5], Yougen Hu[2], Huanjun Chen[1,4] ✉, and Xuchun Gui[1] ✉

[1] State Key Laboratory of Optoelectronic Materials and Technologies, School of Electronics and Information Technology, Sun Yat-sen University, Guangzhou 510275, China
[2] National Key Laboratory of Materials for Integrated Circuits, Shenzhen Institute of Advanced Electronic Materials, Shenzhen Institute of Advanced Technology, Chinese Academy of Sciences, Shenzhen 518055, China
[3] China Academy of Aerospace Science and Innovation, Beijing 100176, China
[4] Guangdong Province Key Laboratory of Display Material and Technology, Guangzhou 510275, China
[5] School of Materials Science and Engineering, Sun Yat-sen University, Guangzhou 510275, China

Cite this article: *Nano Research*, **2025**, *18*, 94907041. https://doi.org/10.26599/NR.2025.94907041

ABSTRACT: Electromagnetic interference (EMI) shielding in high-frequency range, especially the rapidly growing terahertz (THz) frequency range, attracts increasing attention due to the potential application of terahertz in 6G wireless communication, and security inspection. However, traditional conductive EMI films typically achieve high shielding effectiveness through strong reflection, which may cause secondary pollution to other devices. Here, a gradient structure strategy was proposed to construct $Ti_3C_2T_x$/hydroxypropyl methyl cellulose (HPMC) film, in which the content of $Ti_3C_2T_x$ gradually increases along the thickness direction, resulting in different conductivity of the two surfaces (surface-M and surface-H) for the film. The obtained gradient-film exhibits an EMI shielding efficiency of over 48.5 dB in the THz range (0.2–1.6 THz) at a thickness of 40 μm. Especially, as the THz waves incident from the surface-H to the film, the absorption effectiveness reaches 48.2 dB (average absorbed power loss up to 91.4%), and the reflection effectiveness is only 0.3 dB. In additions, the gradient-film also demonstrates a high absorption rate of 95.5% in the infrared band (2.5–16.7 μm). Moreover, the gradient-film exhibits an excellent tensile stress and Young's modulus value of 173.1 MPa and 2.8 GPa, respectively. Therefore, the gradient-film proposed in this work, with excellent electromagnetic absorption in both THz and infrared band, provides a promising candidate for the next-generation EMI shielding applications.

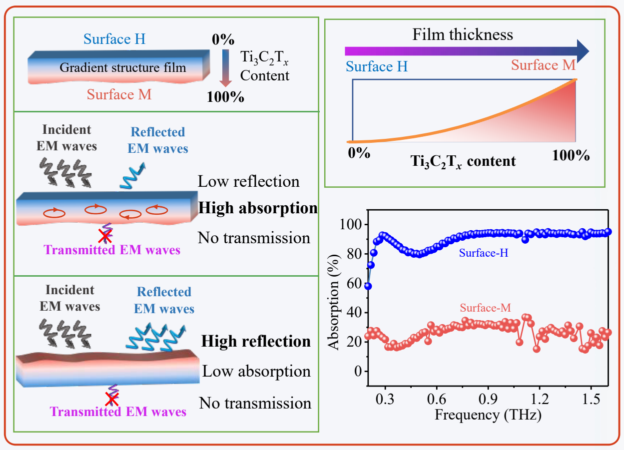

KEYWORDS: electromagnetic interference shielding, Janus film, terahertz, MXene

1 Introduction

In recent years, terahertz (THz) technology (within 0.1–10 THz) has attracted increasing attention due to its potential applications in radar systems, 6G wireless communication, and security inspection, etc. [1–5]. With the rapid development of terahertz electronic devices, there is an increasing demand for THz electromagnetic interference (EMI) shielding films to deal with electromagnetic radiation, interference, and information leakage [6–10]. According to transmission line theory, EMI shielding films mainly achieve shielding and isolation of incident electromagnetic waves through surface reflection and internal absorption [11–15]. The transmittance (T) of electromagnetic wave is the deduction of reflection (R) and absorption (A) by the total power, as is expressed in equation: $T = 1 - R - A$ [16]. For the high conductivity electromagnetic shielding films, such as graphene, carbon nanotubes (CNTs), and MXene, it usually reflects most of the

Received: August 2, 2024; **Revised:** September 5, 2024
Accepted: September 18, 2024

✉Address correspondence to Xuchun Gui, guixch@mail.sysu.edu.cn; Huanjun Chen, chenhj8@mail.sysu.edu.cn

power loss of the incident electromagnetic wave onto the surface to achieve high EMI shielding efficiency (EMI SE), due to the surface impedance mismatch [17–19]. For example, the 40-μm MXene film reflected more than 97% of the electromagnetic waves, reaching an impressive EMI SE of up to 116.2 dB [19]. And a 4-μm MXene-based film was provided with more than 95% reflection loss, achieving a high EMI SE of 71.4 dB in the frequency of 0.2–1.6 THz [8]. However, these high-conductivity two-dimensional (2D) nanosheets shielding films have achieved excellent EMI SE through strong reflection, the reflected electromagnetic waves may cause secondary pollution to other devices.

In order to ensure high EMI SE while reducing *R*, it is necessary to improve the *A* of electromagnetic waves by the shielding film. At present, assembling 2D nanosheets into films with porous network or gel structure is an effective strategy to improve their absorption for electromagnetic wave [11, 20–25]. For example, the MXene-based shielding films with porous network structure exhibited an EMI SE of 51 dB for THz wave at a thickness of 85 μm. But, the refection loss (RL) is only 10 dB [10]. A 130-μm hydrogel-type MXene-based shielding film showed an EMI SE of over 45.3 dB in the 0.2–2.0 THz, and refection loss of 23.2 dB [9]. The 1.0-mm MXene-based hybrid aerogels film was able to dissipate nearly 99% of the energy of the incident electromagnetic wave inside the shielding film, resulting in an EMI SE value of 57.5 dB in the ranging from 0.5 to 3.0 THz [26]. However, the strategies such as pore-forming or gels inevitably increase the thickness of the shielding film, which restricts its application in electronic devices with high integration. In addition, constructing shielding film with metasurface can enhance absorption loss within a limited thickness, but only at special frequencies and a narrow bandwidth [27–31]. For example, the carbon-based film with three-dimensional (3D) metasurface microstructures demonstrated a RL of 43.7 dB only at 1.06 THz [32]. A metamaterial layer with H-shaped arrays exhibits sharp resonance at about 1.4 THz with the absorption of 70% [33]. Therefore, it is still challenging to greatly improve the wide-band absorption of shielding film with limited thickness.

Here, a gradient-film is prepared by continuously varying the mass ratio of $Ti_3C_2T_x$ nanosheets and hydroxypropyl methyl cellulose (HPMC) along the film thickness direction, in which the content of $Ti_3C_2T_x$ nanosheets gradually increases from one surface (0 wt.%) to the opposite surface (100 wt.%), giving rise to a discernible longitudinal gradient in conductivity, as illustrated in Fig. 1(a). Therefore, the gradient film exhibits two surfaces with completely different properties, namely the highly conductive $Ti_3C_2T_x$ MXene surface (surface-M) and the insulating HPMC surface (surface-H). These two surfaces exhibit different responses to the incident THz electromagnetic waves, as illustrated in Fig. 1(a). The longitudinal gradient in electrical conductivity plays a pivotal role in enabling the gradient film to attain high EMI SE and broadband absorption of THz waves. Consequently, the gradient-film delivered an average EMI SE of 48.5 dB for THz waves within the frequency range of 0.2–1.6 THz at a thickness of 40 μm. Additionally, the film exhibited a remarkable absorption capability, reaching an absorption rate of 91.4% for incident electromagnetic wave energy. Furthermore, the gradient-film also possessed an absorption rate of 95.5% in the infrared spectral band (2.5–16.7 μm). Notably, HPMC not only participates in the regulation of the film's longitudinal conductivity but also forms bonding interactions with MXene nanosheets. As a result, the tensile stress of the gradient-film increases by 400% compared to the MXene film. Therefore, the gradient structure design provides an effective method for preparing robust EMI shielding materials with strong EM field absorption.

2 Results and discussion

2.1 Fabrication and characterization of gradient-film

Figure 1(b) illustrates the longitudinal cross-section of the gradient-film. As a comparison, we also prepared mixed-film and partially-gradient-film. In the gradient-film, the content of $Ti_3C_2T_x$ nanosheets increases from 0 wt.% in surface-H to 100 wt.% in surface-M, and the increase rate is related to total weight ratio of $Ti_3C_2T_x$ nanosheets/HPMC. M1H1, M1H5, M1H10, and M1H15 gradient-films correspond to different total weight ratios of $Ti_3C_2T_x$ nanosheets/HPMC, namely 1:1, 1:5, 1:10, and 1:15, respectively. In the mixed-films, the $Ti_3C_2T_x$ nanosheets are uniformly mixed with HPMC, resulting in a uniform distribution of $Ti_3C_2T_x$ nanosheets

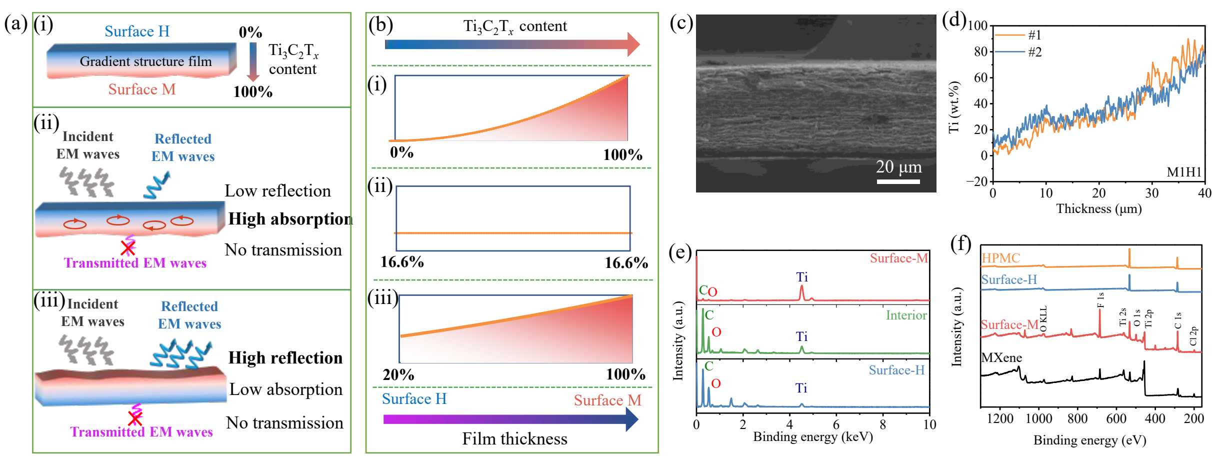

Figure 1 Structural and micromorphology characterization of the gradient-film. (a) Schematic diagram of the interaction between gradient-film and electromagnetic waves: (i) The content of $Ti_3C_2T_x$ in the film varies continuously from surface-H to surface-M; (ii) as the terahertz waves incident from the surface-H, it exhibits low reflection and strong absorption; (iii) as the terahertz waves incident from the surface-M, it exhibits strong reflection and low absorption. (b) Schematic diagram illustrating the cross-section of the $Ti_3C_2T_x$ nanosheets proportions for the internal structure of gradient-film (i), mixed-film (ii), and partially-gradient-film (iii). (c) Cross-sectional SEM image of gradient-film. (d) Liner EDS results of the cross-section of H1M1 gradient-film. (e) EDS results of surface-M, interior, surface-H of gradient-film. (f) XPS results of surface-M, surface-H, HPMC and $Ti_3C_2T_x$ nanosheets.

throughout the films with a weight percent of 16.6%. The internal structure of the partially-gradient-film is similar to that of the gradient-film, where the content of $Ti_3C_2T_x$ nanosheets also gradually increases. However, unlike the gradient-film, the content of $Ti_3C_2T_x$ nanosheets in surface-H does not increase from 0, but rather from a specific value (such as 20 wt.% in Fig. 1(b)(iii)). More details of preparation methods for all films are shown in experimental section.

The $Ti_3C_2T_x$ nanosheets, obtained through solution etching, exhibit a diverse range of functional groups on their surfaces, facilitating effective bonding with HPMC (Fig. S1(a) in the Electronic Supplementary Material (ESM)). The crystal structures of gradient-film and $Ti_3C_2T_x$ film were determined by X-ray diffraction (XRD) in Fig. S1(b) in the ESM, the characteristic peak (002) of $Ti_3C_2T_x$ film signifies that the Al layer has been successfully etched away from the Ti_3AlC_2 (MAX) to obtain the $Ti_3C_2T_x$ nanosheets. Compared with $Ti_3C_2T_x$ film, when combined with HPMC, the (002) peak of the gradient-film is shifted from $2\theta = 7.7°$ to 6.4°, indicating that HPMC has been intercalated between the $Ti_3C_2T_x$ nanosheets, and the *c*-lattice parameter has been enlarged [34]. In addition, a narrower full-width at half-maximum (FWHM) indicates a more orderly arrangement of $Ti_3C_2T_x$ nanosheets in the gradient-film. The typical characteristic peaks of 199 and 283 cm^{-1} in the Raman spectra further indicate the successful preparation of $Ti_3C_2T_x$ nanosheets [35]. The ordered arrangement of $Ti_3C_2T_x$ nanosheets at a thickness of approximately 40 μm is directly observed in the cross-sectional scanning electron microscopy (SEM) images of the gradient-film (Fig. 1(c) and Fig. S2 in the ESM).

Linear-scanning energy dispersive spectrometer (EDS) is used to investigate the element content along the cross-section of the gradient-film and mixed-film. The EDS results corresponding to the cross-section of the gradient-film are shown in Fig. 1(d). The proportion of Ti element increases linearly with the film's thickness, indicating that the $Ti_3C_2T_x$/HPMC film has a continuous gradient variation in the content of $Ti_3C_2T_x$ nanosheets. The increase rate is related to weight ratio of $Ti_3C_2T_x$ nanosheets/HPMC (Fig. S3 in the ESM). The proportion of Ti element in the surface-M is more than 80 wt.%, indicating that the surface-M is composed of high-conductivity $Ti_3C_2T_x$ nanosheets. On the contrary, the Ti peak does not appear in the EDS from the surface-H, verifying that the surface-H is composed of insulating HPMC (Fig. 1(e)). Furthermore, the EDS mapping images of gradient-film further indicate the uniform distribution of $Ti_3C_2T_x$ nanosheets in the surface-M (Fig. S4 in the ESM). However, the proportion of the Ti element remains relatively constant throughout the entire mixed-film, indicating a uniform blending of $Ti_3C_2T_x$ and HPMC (Figs. S5 and S6 in the ESM).

Figure 1(f) provides the X-ray photoelectron spectroscopy (XPS) results of pristine HPMC, pristine $Ti_3C_2T_x$ film, and gradient-film. The XPS spectrum of the surface-M resembles that of pristine $Ti_3C_2T_x$ film, while the surface-H and the pristine HPMC are also similar with each other. Meanwhile, the Ti–C doublet peak (454.5 and 460.4 eV) and Ti–O doublet peak (458.8 and 463.5 eV) are detected in the Ti 2p spectra of surface-H (Fig. S7 in the ESM) [36]. The results from both EDS and XPS confirmed the successful preparation of $Ti_3C_2T_x$/HPMC gradient-film, showing two markedly distinct surfaces. More importantly, the content of $Ti_3C_2T_x$ nanosheets directly affects the longitudinal resistance of the gradient-film. The conductivity of the gradient-film, which is crucial for improving impedance matching to induce and dissipate THz electromagnetic waves within the gradient-film, also varies with the $Ti_3C_2T_x$ nanosheets content. As shown in Table S1 in the ESM, the sheet resistance of the surface-M is about 300 mΩ/□, whereas that of the surface-H surpasses the measuring device's range limit. This confirms a longitudinal increase in resistance from the surface-M to the surface-H of the gradient-film.

2.2 EMI shielding performances of the film

To understand the influence of the longitudinal impedance of the gradient-film on the THz EMI shielding, the THz waves illuminated from different surfaces of the gradient-film are analyzed. The average EMI SE values in the frequency range of 0.2–1.6 THz of the surface-M and the surface-H of M1H5 gradient-film are 48.9 and 48.5 dB, respectively (Fig. S8 in the ESM). These results show that the incidence direction of electromagnetic waves has no significant effect on EMI SE. Moreover, when THz waves incident from surface-H, the EMI absorption effectiveness (SE_A) and reflection effectiveness (SE_R) of gradient-film are 48.2 and 0.3 dB, respectively (Fig. 2(a)). The values of EMI SE, SE_R, and SE_A illustrate the incident THz electromagnetic wave has almost no reflection loss and transmission, which means that the power of THz electromagnetic waves is dissipated by the gradient-film. The average absorbed power loss of surface-H is 91.4%, much higher than the value of 25.5% of the surface-M (Fig. 2(b)). The absorption process can be described as: Firstly, the incident THz electromagnetic waves penetrate surface-H without loss due to an undifferentiated matched impedance between the surface and air. Subsequently, the THz waves are gradually absorbed within the gradient film. Finally, the unabsorbed THz waves are transmitted to the surface M and reflected. And the reflected THz waves could be dissipated again inside the gradient-film. The THz electromagnetic wave consumption process, called "absorb–reflect–reabsorb" process, is based on the mechanism of gradual conductivity to achieve high absorption of THz electromagnetic waves. However, when THz electromagnetic waves incident from surface-M, it is reflected directly on the surface, resulting in similar EMI SE, but with a low absorption loss.

The relationships between the EMI SE and the $Ti_3C_2T_x$ nanosheets content in different $Ti_3C_2T_x$/HPMC gradient-film of the same thickness are shown in Fig. 2(c) (more detailed EMI SE curves are shown in Fig. S8(b) in the ESM). Specifically, the EMI SE values of gradient-film with different ratios are 53.0 dB (M1H1), 48.5 dB (M1H5), 33.2 dB (M1H10), and 25.4 dB (M1H15), respectively. The EMI SE value depends on the overall conductivity of the films (Fig. S9 in the ESM). For M1H1, M1H5, M1H10, and M1H15 film, the average absorbed power losses are 78.1%, 91.4%, 95.3%, and 97.2% respectively, much higher than that of the THz wave incident from surface-M (Fig. 2(d)). Detailed absorption curves of gradient-film with different ratio are shown in Fig. S10 in the ESM.

Despite a gradual increase in absorption loss against a higher proportion of HPMC, the EMI SE value of gradient-films decreases more significantly. To further verify the EMI shielding performance of the gradient-film in the GHz band, the illumination frequency is reduced to 8.2–40.0 GHz, including the X band, Ku band, K band, and Ka band (Fig. S11 in the ESM). The M1H1 gradient-film also exhibits a highest EMI SE value of 57.1 dB, significantly higher than 31.5 dB of mixed-film with the same thickness (Fig. S12 in the ESM). The EMI SE, SE_A, and SE_R for surface-M were 39.2, 26.2 and 13.0 dB within the range of 8.2–12.4 GHz, respectively. The 26.2 dB SE_A means that only 5.0% of the incident EM wave is absorbed by

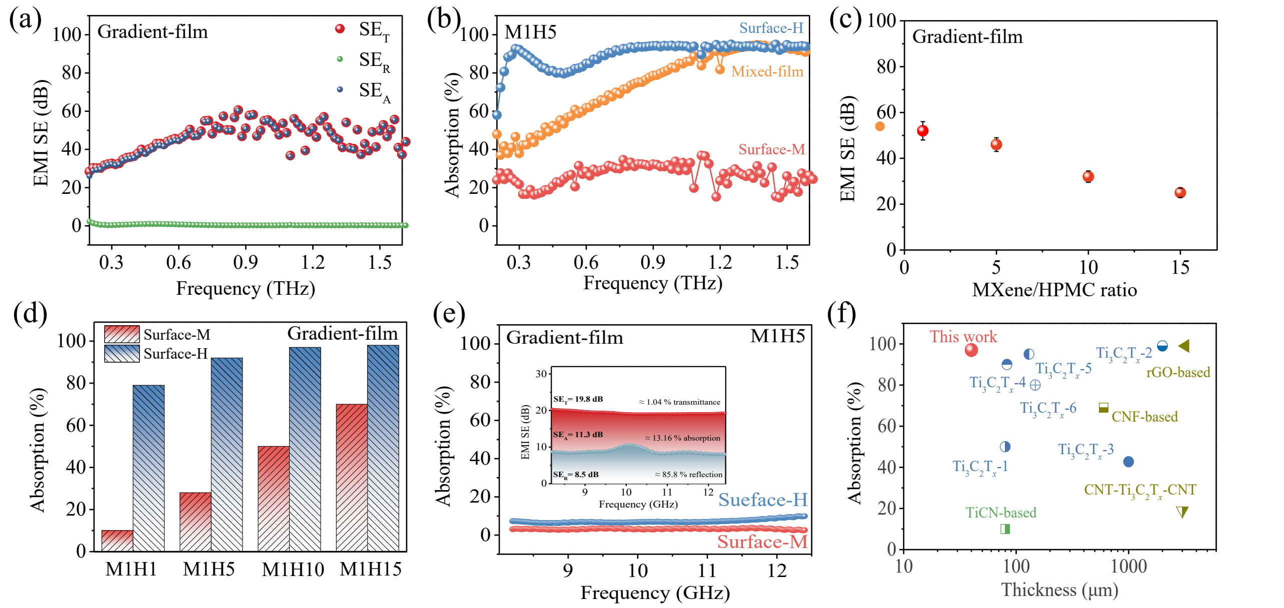

Figure 2 Electromagnetic interference shielding performance of the gradient-films (all the tested samples had a thickness of 40 μm). (a) Total EMI SE$_T$, SE$_R$, SE$_A$ of gradient-film in the frequency range of 0.2–1.6 THz (the SE$_T$ includes the reflection and absorption parts). (b) The absorption loss of M1H5 mixed-film, surface-M, and surface-H of M1H5 gradient-film. (c) The average values of total EMI SE (SE$_T$) in gradient-film with different $Ti_3C_2T_x$/HPMC ratios in the frequency range of 0.2–1.6 THz. (d) The average absorption loss values of surface-M and surface-H in gradient-film with different $Ti_3C_2T_x$/HPMC ratios in the frequency range of 0.2–1.6 THz. (e) The absorption loss of surface-M and surface-H of M1H5 gradient-film in the frequency range of 8.2–12.4 GHz, inset showing total EMI SE, SE$_R$, SE$_A$ of gradient-film. (f) Comparison of the absorption loss vs. thickness between gradient-film, and other THz shielding materials (detailed data thereof are listed in Table S2 in the ESM).

the film (Fig. 2(e)). Both surface-M and surface-H of the gradient-film mainly reflect GHz electromagnetic waves to achieve high EMI SE (Fig. S13 in the ESM). Finally, to highlight the superior THz electromagnetic wave absorption loss of the gradient-film, the absorbed power loss value as a function of thickness in this work is compared with those of other currently reported THz shielding materials (Fig. 2(f)) [9, 22, 26, 37–42]. Obviously, the gradient-film exhibits excellent absorption loss (91.4% of M1H5) with the thickness of 40 μm, which is much better than other THz electromagnetic wave shielding materials, such as MXene films, CNTs films, and graphene films.

To gain a more intuitive understanding the effect of gradient-film on GHz and THz electromagnetic fields, the interactions between the incident electromagnetic wave at different ports and gradient-films were simulated by COMSOL. The simulation model is shown in the Fig. 3(a), and the specific parameters can be checked in the ESM, where it can be seen that the shielding films divide the rectangular waveguide cavity into two regions. The surface-H is positioned towards the port 1, while surface-M towards the port 2. The port 1 serves as the transmitting electromagnetic wave port, and the electromagnetic wave will enter the gradient-film from the surface-H, and port 2 serves as the receiving port to capture the transmitted electromagnetic wave. The modeling results clearly showed that the transmitting region exhibits a high electric field intensity (deep red area), while there is no signal in the receiving region (deep blue area), further confirming that both THz and GHz electromagnetic wave will be blocked by the gradient-films (Fig. 3(b)). Moreover, within the THz band, the electric field intensity in the gradient-films gradually degrades from the surface-H to the surface-M, indicating the energy of THz electromagnetic waves is consumed in the gradient-films. The power of incident THz electromagnetic waves decreases continuously inside the gradient-film after penetrating the surface-H without damage, resulting in high absorption, low reflection, and low transmittance of THz electromagnetic waves. In addition, the simulated absorption, transmission, and reflection in the ranges of GHz and THz bands are consistent with the real values obtained from the experiment, further validating the reliability of the results (Fig. 3(c)). Moreover, according to the results of simulations and experimental measurements, the higher-frequency electromagnetic waves are more easily absorbed by the gradient-film, owing to that electromagnetic waves with shorter wavelengths are more easily to interact with the $Ti_3C_2T_x$ nanosheets.

On the contrary, when port 2 serves as the electromagnetic wave transmitting port, the electromagnetic wave will enter the gradient-films from the surface-M (Fig. 3(d)). The transmitting region also exhibits a high electric field intensity. Conversely, both the receiving region and the interior region within the gradient film do not exhibit such intensity (Fig. 3(e)). This observation further validates that the THz waves will be reflected on surface-M and obstructed by the films. However, regardless of the direction of the incident GHz electromagnetic wave, the gradient-film does not exhibit excellent absorption properties, verifying previous conclusion that the EMI SE of gradient-films are dominated by reflection loss (Fig. 3(f)). The reflection power loss (R) of GHz and THz electromagnetic waves on surface-M and surface-H can be calculated using the Eqs. (1) and (2)

$$\eta_c = \sqrt{\frac{\mu_0}{\varepsilon - \frac{j\sigma}{2\pi f}}} \tag{1}$$

$$R = \left| \frac{\eta_c - \eta_0}{\eta_c + \eta_0} \right|^2 \tag{2}$$

where η_c is the surface impedance of film, η_0 is the impedance of air, μ_0 is the permeability of the film, ε is the dielectric constant of

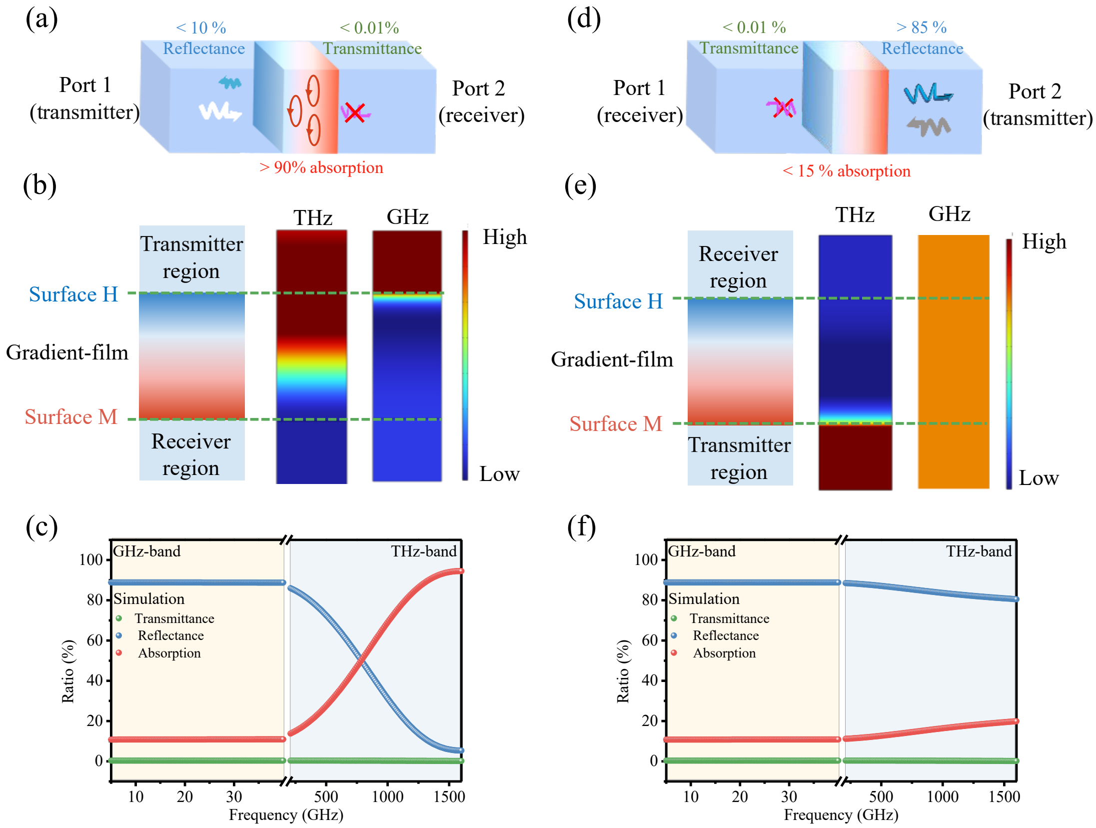

Figure 3 Simulated THz and GHz EMI of gradient-film with different incident directions. (a) Schematic diagram of the simulation model of incident electromagnetic wave entering from surface-H. (b) Simulation results in the frequencies of 10 GHz and 1.5 THz, and (c) the calculation results of power loss within 5.0–40.0 GHz and 0.2–1.6 THz for gradient-film from simulation model in (a). (d) Schematic diagram of the simulation model of incident electromagnetic wave entering from surface-M. (e) Simulation results in the frequencies of 10 GHz and 1.5 THz, and (f) the calculation results of power loss within 5.0–40.0 GHz and 0.2–1.6 THz for gradient-film from simulation model in (d).

the film, σ is the surface conductivity of the film, and f is the frequency of the electromagnetic waves (10.0 GHz or 1.0 THz). According to Eqs. (1) and (2), the reflection power loss (R) of gradient films for THz and GHz electromagnetic waves mainly depends on the surface conductivity of the film and the frequency of the electromagnetic waves. According to the simulation and experimental results, the equivalent conductivity of the surface-M is defined as 20,000 S/m, while that of the surface-H is 200 S/m. The calculated absorption losses of the gradient-film are lower than 0.15 in the GHz, which is consistent with the experimental data and simulation result. However, in the THz band, the calculated absorption loss of the gradient-film is 0.83, much higher than 0.14 of surface-M, further validating the previously proposed concept of the "absorb–reflect–reabsorb" process.

The M1H5 gradient-films exhibit the excellent EMI SE with a high absorption loss, making them suitable for exploring other properties of gradient-film. As shown in Fig. 4(a), the EMI SE value of gradient-film increases with the thickness (Fig. S14 in the ESM), reaching a high EMI SE up to 58.5 dB at the thickness of 55 μm. Detailed EMI SE curves within the 0.2–1.6 THz range of gradient-films of various thicknesses are provided in Fig. S15 in the ESM. Furthermore, the absorption value also increases with thickness of gradient-films, while that associated with the surface-M shows the opposite trend (Fig. 4(b)). As a result, with the increasing thickness of the gradient film, the disparity in the response to THz waves between the two surfaces becomes more noticeable. This means that increasing the thickness of the gradient-film is a simple approach to fabricating an excellent EMI SE shielding film with high absorption loss. The EMI SE values of partially-gradient-films decrease with the proportion of $Ti_3C_2T_x$ nanosheets on the initial surface, which is related to the overall electrical conductivity of the partially-gradient-film (Fig. 4(c)). As shown in Fig. 4(d), the reflection of the incident THz waves increases from 60% to 100% (the initial content of $Ti_3C_2T_x$ nanosheets on the surface of surface-H is 60 wt.%) partially-gradient-film, preventing them from entering the interior of the partially-gradient-film. However, reducing the $Ti_3C_2T_x$ nanosheets content in the surface of surface-H of the partially-gradient-film can reduce the impedance mismatch and enhance THz wave absorption loss.

2.3 Infrared emission performances of the film

To explore the comprehensive characteristics of the various fabricated films over a wide infrared wavelength range (2.5–16.7 μm), their thermal emission properties were evaluated using Fourier transform infrared (FTIR) spectrometers equipped with an integrating sphere (Fig. 5(a)). According to previous report [43], $Ti_3C_2T_x$ film is provided with a high damping constant and low refractive index, similar to metallic materials, resulting in the high infrared light reflection over a wide wavelength range. The aforementioned experimental results demonstrate that the absorption value of gradient-film in surface-H is 95.5%, much higher than that of the surface-M (43.2%), confirming that gradient-film is also provided with high absorption in the infrared band of 2.5–16.7 μm (Fig. 5(b)). The terminal active groups on the surface

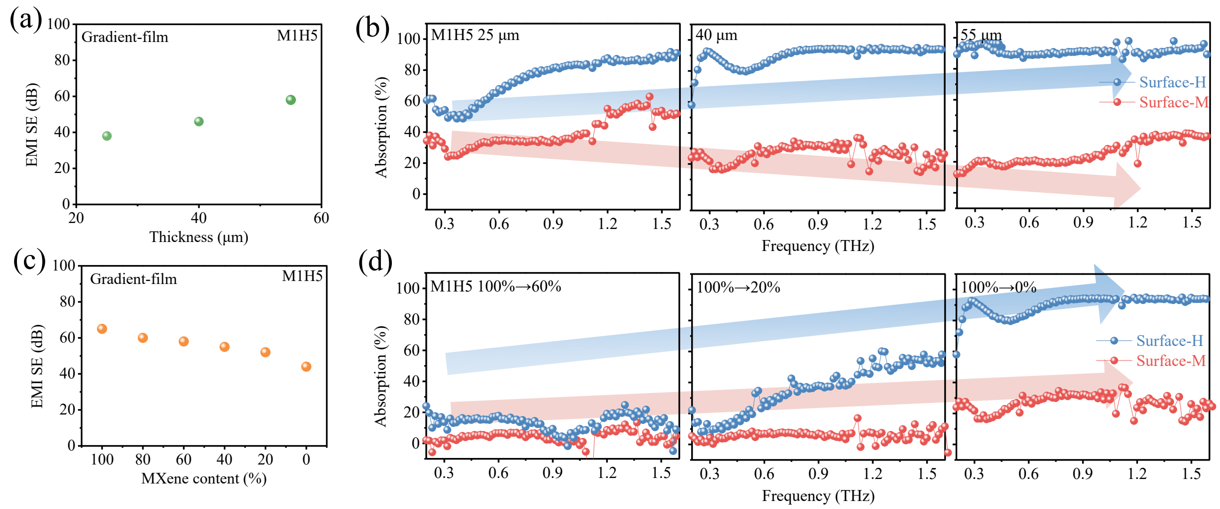

Figure 4 THz electromagnetic wave shielding performance of the M1H5 gradient-film with different thicknesses and partially-gradient-films in the frequency range of 0.2–1.6 THz. (a) The average total EMI SE values of gradient-film with different thicknesses. (b) The absorption loss of surface-M and surface-H of gradient-film with different thicknesses. (c) The average values of total EMI SE in partially-gradient-films with different initial surface. (d) The average absorption loss values of surface-M and initial surface partially-gradient-films with different initial surface.

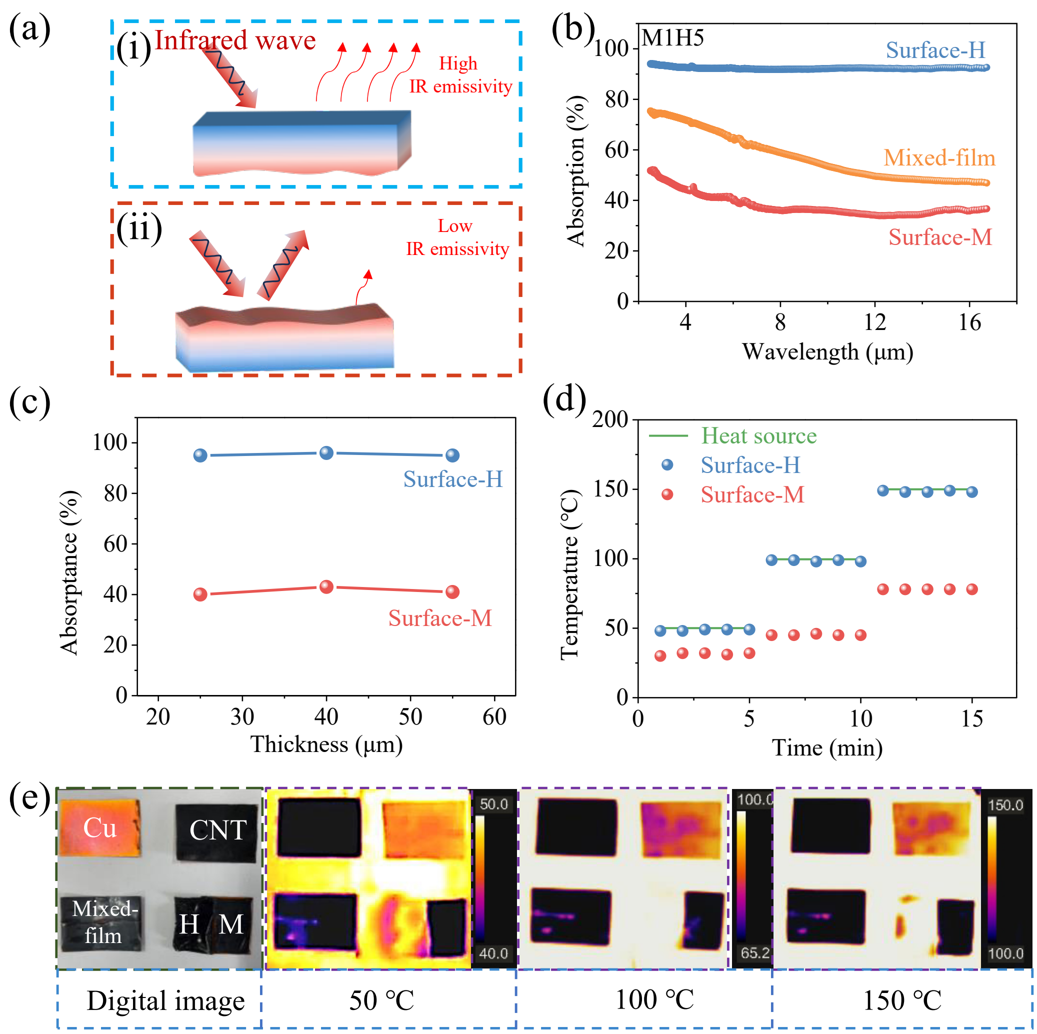

Figure 5 Infrared electromagnetic wave absorptive performance of M1H5 gradient-film. (a) Schematic diagram of the gradient-film, where incident THz waves can be highly absorbed by surface-H, but also can be lowly by surface-M. (b) The absorption of mixed-film, surface-M, and surface-H of gradient-film with the infrared band of 2.5–16.7 μm. (c) The average values of absorption of surface-M and surface-H for gradient-film with different thicknesses. (d) Temperature versus time of the heat source, surface-H and surface-M of gradient-film. (e) IR photographs of the Cu, CNTs, mixed-film, surface-H, and surface-M of gradient-film on a hot plate with a constant temperature of 50, 100, and 150 °C.

of $Ti_3C_2T_x$ nanosheets, such as –F, –OH, and –O, demonstrate the ability to absorb infrared electromagnetic waves [43]. Additionally, the molecular chains of HPMC can achieve strong absorption losses for infrared electromagnetic waves through various functional groups, including –OH, C–O–C, and C–H [44]. Unlike the Cu film or pristine $Ti_3C_2T_x$ film, the gradient-film can absorb most of the energy of infrared waves, similar to a black absorber made up of CNT film. Moreover, the average absorption values of the gradient-films (the surface-H and surface-M) with varying thicknesses including 20, 40, and 55 μm are shown in Fig. 5(c). Clearly, the absorption of the gradient-films is independent of the film thickness within the considered range. In addition, after the gradient-film is divided into two halves, the surface-H and surface-M were heated to 50, 100, and 150 °C and held there for 5 min using a thermal stage. The temperatures of the thermal stage, the surface-H, and the surface-M are shown in Fig. 5(d). The temperatures of surface-H measured at 49.0, 98.5, and 149.3 °C, corresponding to thermal stage of 50, 100 and 150 °C, respectively. However, the temperatures of the surface-M are 31.5, 45.5, and 78.0 °C, much lower than that of the thermal stage. The result further verifies that the surface-H of gradient-film possesses the high-absorptivity in the infrared band ranging from 2.5 to 16.7 μm, while the surface-M reflects most of the infrared wave. The infrared radiation images for gradient-films, mixed-films, CNT film, and Cu film at 50, 100, and 150 °C were captured by an infrared thermal camera (Fig. 5(e)). The surface-H, like the CNT film, can be detected at higher temperatures of all testing temperatures, intuitively demonstrating the surface-H is equipped with high absorptivity of infrared band. While the surface-M, mixed-film, and Cu metal remain notably cooler than the surface-H and CNT film, this temperature difference makes them less detectable by the infrared thermal camera imaging, primarily due to their limited thermal radiation. Most interestingly, gradient-film could not only be used as an infrared absorption device (high-absorptivity, surface-H), but also effectively hide itself from infrared detection (limited thermal radiation, surface-M).

Mechanical properties serve as crucial indicators in determining the extensive applicability of gradient-films. The tensile stress–strain curves of gradient-film are shown in Fig. S16(a) in the ESM. The M1H5, M1H10, and M1H15 gradient-film exhibit remarkable tensile stress and tensile strain separately of 173.1, 183.1, 167.8 MPa, and 6.9%, 9.2%, 12.5% at the film thickness of approximately 40 μm, which are superior to the M1H1 gradient-film and pristine $Ti_3C_2T_x$ film. These results confirm that the HPMC has the capability to enhance the arrangement of $Ti_3C_2T_x$ nanosheets and form hydrogen bonds with them. This interaction contributes to the improvement in the mechanical properties of the gradient film, as illustrated in Fig. S16(b) in the ESM. In addition, the calculated Young's modulus and toughness versus $Ti_3C_2T_x$ nanosheets content in different $Ti_3C_2T_x$/HPMC gradient-film are shown in Fig. S16(c) in the ESM. The highest Young's modulus of 2.8 GPa and highest toughness of 17.05 MJ/m^3 were attained with M1H5 and M1H15. Obviously, the addition of HPMC comprehensively improves the mechanical properties of the gradient-film, enabling its flexibility and applicability.

3 Conclusions

In summary, we report a novel assembly process to construct $Ti_3C_2T_x$/HPMC gradient-films with longitudinal gradient conductivity for electromagnetic interference shielding. The "absorb–reflect–reabsorb" process exhibited by the gradient-films greatly improved the absorption loss. After undergoing the "absorb–reflect–reabsorb" process, the gradient-film achieved a power loss coefficient of *A* close to 0.91 within the frequency range of 0.2–1.6 THz. Furthermore, the gradient-film demonstrated an absorption loss value of 95.5% in the infrared band of 2.5–16.7 μm. Additionally, the tensile stress value of the M1H5 gradient-film is an excellent 173.1 MPa, 400% higher than that of pristine $Ti_3C_2T_x$ film. Thus, the ultra-thin and high-EMI SE gradient-film hold tremendous potential for applications in the fields of sophisticated and miniaturized THz electronic devices.

4 Experimental section

4.1 Preparation of $Ti_3C_2T_x$ nanosheets and HPMC solution

$Ti_3C_2T_x$ nanosheets were obtained by etching the Ti_3AlC_2 (MAX) precursor powder. Firstly, 2 g LiF was dissolved in 30 mL 9 M HCl solution in a polytetrafluoroethylene container and stirred for 0.5 h at 35 °C. Then, the 2 g MAX powder was slowly added to the mixing solution and continuously stirred for 24 h for etching Al from Ti_3AlC_2. The rinsed reactants were freeze-dried for 24 h to obtain $Ti_3C_2T_x$/Ti_3AlC_2 sediment powder. Finally, sediment powder was added to deionized water, centrifuged at 8000 rpm after ultrasound, and the $Ti_3C_2T_x$ nanosheets powder was obtained after freezing. HPMC solution was obtained by adding HPMC powder to deionized water and stirring continuously for 12 h at 60 °C.

4.2 Preparation of $Ti_3C_2T_x$/HPMC gradient-film, mixed-film, and partially-gradient-film

For the preparation of gradient-film, the $Ti_3C_2T_x$ nanosheets powder (9.4–75 mg) was dispersed in deionized water, ultrasonic for 30 min, and then poured into the vacuum filtration container. During the filtration process, 40 mL HPMC solution (concentration 1.75–3.5 mg/mL) was continuously injected at a rate of 2 mL/h into the $Ti_3C_2T_x$ nanosheets solution using a syringe pump. The gradient-films were obtained by directly stripping from the filter paper. These gradient-films exhibited increasing $Ti_3C_2T_x$ nanosheet concentration from the surface-H to the surface-M.

For the preparation of mixed-film, 10 mL $Ti_3C_2T_x$ nanosheets solution (0.94–7.5 mg/mL) was added into 40 mL HPMC solution (1.75–3.5 mg/mL) with ultrasonic stirring for 30 min. Subsequently, the mixture was treated by a vacuum filtration for fabricating the mixed-films. Partially-gradient-films were achieved by adjusting the proportion of $Ti_3C_2T_x$ nanosheets/HPMC and the injection rate of HPMC solution. The fabricating method for partially-gradient-films followed a similar approach to that of gradient-films, with the difference being the replacement of the surface-H with a surface featuring a different proportion of nanosheets/HPMC content. The 80 wt.% to 100 wt.%, 60 wt.% to 100 wt.%, 40 wt.% to 100 wt.%, 20 wt.% to 100 wt.%, and 0 wt.% to 100 wt.% partially-gradient-films corresponded to films where, in addition to the $Ti_3C_2T_x$ nanosheets content on the surface-M remaining at 100 wt.%, the contents on the initial surface were 80 wt.%, 60 wt.%, 40 wt.%, 20 wt.%, and 0 wt.%, respectively.

4.3 Characterization

The micromorphology of the $Ti_3C_2T_x$ nanosheets, mixed-film, and gradient-film were investigated by field-emission SEM (FE-SEM, Hitachi, S-4800). The element contents of the surface-M and surface-M of gradient-film and mixed-film were investigated by EDS equipped on SEM systems. XRD (Bruker, D8 ADVANCE) with Cu Kα radiation was used to measure the structures of $Ti_3C_2T_x$ nanosheets and gradient-film. The chemical bonds and chemical states of the samples $Ti_3C_2T_x$ nanosheets, $Ti_3C_2T_x$ film and gradient-film were analyzed by Raman spectrometry (HORIBA, LabRAM HR) and XPS (Thermo Scientific, ESCALAB 250Xi). The EMI SE in the GHz band (8.2–40.0 GHz) and THz band (0.2–1.6 THz) were measured in air using a network analyzer (N5232, VNA, Keysight), and a fiber-coupled THz time-domain spectroscopy system (THz-TDS; BATOP, TDS 1008), respectively. In the THz shielding test, the air absorption loss of THz electromagnetic wave was first tested and set as a reference value. The actual THz shielding effectiveness of samples was obtained by deducting the reference value from the measured THz shielding results. The COMSOL software was used to carry out the simulation of the electromagnetic wave shielding process. The temperatures were determined, and the infrared images were captured by infrared thermal imager (Hikmicro, K-20). The absorption of samples in the infrared band was measured evaluated using FTIR spectrometers equipped with integrating spheres (Bruker, Vertex, 70). The mechanical properties were tested on a universal testing machine (Instron, 5943). Detailed sample parameters, test methods, and calculation formulas of all characterizations were shown in the ESM.

Electronic Supplementary Material: Supplementary material (detailed sample parameters and test methods for GHz and THz wave; the specific parameters and methods of electromagnetic simulation by COMSOL software; micromorphology characterization of the $Ti_3C_2T_x$ nanosheets, mixed-film and gradient-film) is available in the online version of this article at https://doi.org/10.26599/NR.2025.94907041.

Data availability

All data needed to support the conclusions in the paper arepresented in the manuscript and the Electronic SupplementaryMaterial. Additional data related to this paper may be requestedfrom the corresponding author upon request

Acknowledgements

This work was financially supported by the National Natural Science Foundation of China (Nos. 52072415, 52371247, and 91963205), and the Research Fund Program of Guangdong Provincial Key Laboratory of Nanophotonic Functional Materials and Devices.

Declaration of competing interest

All the contributing authors report no conflict of interests in this work.

Author contribution statement

S. D. Y.: Data curation, formal analysis, writing-original draft. R. L. Y.: Formal analysis, writing-editing. Z. Q. L. and W. Q. H.: numerical simulations. X. B. L. and R. W.: Data analysis. Z. B. C.: Investigation. Y. J., Z. P. Z., H. J. C., and Y. G. H.: Methodology, data analysis. X. C. G.: Data analysis, writing-review and editing, supervision. All authors discussed the results and reviewed the final manuscript.

Use of AI statement

None.

References

[1] Suzuki, D.; Oda, S.; Kawano, Y. A flexible and wearable terahertz scanner. *Nat. Photonics* **2016**, *10*, 809–813.

[2] Nagatsuma, T.; Ducournau, G.; Renaud, C. C. Advances in terahertz communications accelerated by photonics. *Nat. Photonics* **2016**, *10*, 371–379.

[3] Banks, P. A.; Kleist, E. M.; Ruggiero, M. T. Investigating the function and design of molecular materials through terahertz vibrational spectroscopy. *Nat. Rev. Chem.* **2023**, *7*, 480–495.

[4] Stantchev, R. I.; Sun, B. Q.; Hornett, S. M.; Hobson, P. A.; Gibson, G. M.; Padgett, M. J.; Hendry, E. Noninvasive, near-field terahertz imaging of hidden objects using a single-pixel detector. *Sci. Adv.* **2016**, *2*, e1600190.

[5] Zhao, T.; Xie, P. Y.; Wan, H. J.; Ding, T. P.; Liu, M. Q.; Xie, J. L.; Li, E. N.; Chen, X. Q.; Wang, T. W.; Zhang, Q. et al. Ultrathin MXene assemblies approach the intrinsic absorption limit in the 0.5–10 THz band. *Nat. Photonics* **2023**, *17*, 622–628.

[6] Wan, H. J.; Liu, N.; Tang, J.; Wen, Q. Y.; Xiao, X. Substrate-independent $Ti_3C_2T_x$ MXene waterborne paint for terahertz absorption and shielding. *ACS Nano* **2021**, *15*, 13646–13652.

[7] Li, S. J.; Xu, S. J.; Pan, K. C.; Du, J.; Qiu, J. Ultra-thin broadband terahertz absorption and electromagnetic shielding properties of MXene/rGO composite film. *Carbon* **2022**, *194*, 127–139.

[8] Yang, S. D.; Yang, R. L.; Lin, Z. Q.; Wang, X. M.; Liu, S. J.; Huang, W. B.; Chen, Z. B.; Wei, J. H.; Zeng, Z. P.; Chen, H. J. et al. Ultrathin, flexible, and high-strength polypyrrole/$Ti_3C_2T_x$ film for wide-band gigahertz and terahertz electromagnetic interference shielding. *J. Mater. Chem. A* **2022**, *10*, 23570–23579.

[9] Zhu, Y. Y.; Liu, J.; Guo, T.; Wang, J. J.; Tang, X. Z.; Nicolosi, V. Multifunctional $Ti_3C_2T_x$ MXene composite hydrogels with strain sensitivity toward absorption-dominated electromagnetic-interference shielding. *ACS Nano* **2021**, *15*, 1465–1474.

[10] Lin, Z. H.; Liu, J.; Peng, W.; Zhu, Y. Y.; Zhao, Y.; Jiang, K.; Peng, M.; Tan, Y. W. Highly stable 3D $Ti_3C_2T_x$ MXene-based foam architectures toward high-performance terahertz radiation shielding. *ACS Nano* **2020**, *14*, 2109–2117.

[11] Zhao, B.; Bai, Z. Y.; Lv, H. L.; Yan, Z. K.; Du, Y. Q.; Guo, X. Q.; Zhang, J. C.; Wu, L. M.; Deng, J. S.; Zhang, D. W. et al. Self-healing liquid metal magnetic hydrogels for smart feedback sensors and high-performance electromagnetic shielding. *Nano-Micro Lett.* **2023**, *15*, 79.

[12] Zhao, B.; Du, Y. Q.; Lv, H. L.; Yan, Z. K.; Jian, H.; Chen, G. Y.; Wu, Y. Y.; Fan, B. B.; Zhang, J. C.; Wu, L. M. et al. Liquid-metal-assisted programmed galvanic engineering of core-shell nanohybrids for microwave absorption. *Adv. Funct. Mater.* **2023**, *33*, 2302172.

[13] Zhao, B.; Du, Y. Q.; Yan, Z. K.; Rao, L. J.; Chen, G. Y.; Yuan, M. Y.; Yang, L. T.; Zhang, J. C.; Che, R. C. Structural defects in phase-regulated high-entropy oxides toward superior microwave absorption properties. *Adv. Funct. Mater.* **2023**, *33*, 2209924.

[14] Li, J.; Sun, H.; Yi, S. Q.; Zou, K. K.; Zhang, D.; Zhong, G. J.; Yan, D. X.; Li, Z. M. Flexible polydimethylsiloxane composite with multi-scale conductive network for ultra-strong electromagnetic interference protection. *Nano-Micro Lett.* **2023**, *15*, 15.

[15] Wang, L.; Ma, Z. L.; Qiu, H.; Zhang, Y. L.; Yu, Z.; Gu, J. W. Significantly enhanced electromagnetic interference shielding

performances of epoxy nanocomposites with long-range aligned lamellar structures. *Nano-Micro Lett.* **2022**, *14*, 224.
[16] Iqbal, A.; Sambyal, P.; Koo, C. M. 2D MXenes for electromagnetic shielding: A review. *Adv. Funct. Mater.* **2020**, *30*, 2000883.
[17] Shahzad, F.; Alhabeb, M.; Hatter, C. B.; Anasori, B.; Man Hong, S.; Koo, C. M.; Gogotsi, Y. Electromagnetic interference shielding with 2D transition metal carbides (MXenes). *Science* **2016**, *353*, 1137–1140.
[18] Wan, S. J.; Li, X.; Chen, Y.; Liu, N. N.; Du, Y.; Dou, S. X.; Jiang, L.; Cheng, Q. F. High-strength scalable MXene films through bridging-induced densification. *Science* **2021**, *374*, 96–99.
[19] Iqbal, A.; Shahzad, F.; Hantanasirisakul, K.; Kim, M. K.; Kwon, J.; Hong, J.; Kim, H.; Kim, D.; Gogotsi, Y.; Koo, C. M. Anomalous absorption of electromagnetic waves by 2D transition metal carbonitride Ti_3CNT_x (MXene). *Science* **2020**, *369*, 446–450.
[20] Zhang, Y. L.; Ruan, K. P.; Zhou, K.; Gu, J. W. Controlled distributed $Ti_3C_2T_x$ hollow microspheres on thermally conductive polyimide composite films for excellent electromagnetic interference shielding. *Adv. Mater.* **2023**, *35*, 2211642.
[21] Chen, T. L.; Tian, Y. R.; Guo, Z. H.; Chen, Y.; Qi, Q.; Meng, F. B. Design of novel RGO/2D strip-like ZIF-8/DMAOP ternary hybrid structure towards high-efficiency microwave absorption, active and passive anti-corrosion, and synergistic antibacterial performance. *Nano Res.* **2024**, *17*, 913–926.
[22] Bai, Y.; Qin, F.; Lu, Y. X. Flexible and lightweight Ni/MXene decorated polyurethane sponge composite with sensitive strain sensing performance for ultrahigh terahertz absorption. *Adv. Opt. Mater.* **2022**, *10*, 2101868.
[23] Sang, G. L.; Xu, P.; Yan, T.; Murugadoss, V.; Naik, N.; Ding, Y. S.; Guo, Z. H. Interface engineered microcellular magnetic conductive polyurethane nanocomposite foams for electromagnetic interference shielding. *Nano-Micro Lett.* **2021**, *13*, 153.
[24] Du, Y. Q.; Yan, Z. K.; You, W. B.; Men, Q.; Chen, G. Y.; Lv, X. W.; Wu, Y. Y.; Luo, K. C.; Zhao, B.; Zhang, J. C. et al. Balancing MXene surface termination and interlayer spacing enables superior microwave absorption. *Adv. Funct. Mater.* **2023**, *33*, 2301449.
[25] Peng, H.; He, M.; Zhou, Y. M.; Song, Z. P.; Wang, Y. J.; Feng, S. J.; Chen, X.; Zhang, X.; Chen, H. Low-temperature carbonized biomimetic cellulose nanofiber/MXene composite membrane with excellent microwave absorption performance and tunable absorption bands. *Chem. Eng. J.* **2022**, *433*, 133269.
[26] Xie, Q. D.; Zhao, Y.; Liang, D. F.; Zhang, L. B.; Wen, Q. Y.; Tang, F.; Hu, M.; Deng, L. J.; Zhou, P. H. Lightweight MXene-based hybrid aerogels with ultrabroadband terahertz absorption and anisotropic strain sensitivity. *ACS Appl. Mater. Interfaces* **2022**, *14*, 57008–57015.
[27] Yahiaoui, R.; Chase, Z. A.; Kyaw, C.; Tay, F.; Baydin, A.; Noe, G. T.; Song, J.; Kono, J.; Agrawal, A.; Bamba, M. et al. Dicke-cooperativity-assisted ultrastrong coupling enhancement in terahertz metasurfaces. *Nano Lett.* **2022**, *22*, 9788–9794.
[28] Ding, J.; Xu, N. N.; Ren, H.; Lin, Y. K.; Zhang, W. L.; Zhang, H. L. Dual-wavelength terahertz metasurfaces with independent phase and amplitude control at each wavelength. *Sci. Rep.* **2016**, *6*, 34020.
[29] Squires, A. D.; Gao, X.; Du, J.; Han, Z. J.; Seo, D. H.; Cooper, J. S.; Murdock, A. T.; Lam, S. K. H.; Zhang, T.; van der Laan, T. Electrically tuneable terahertz metasurface enabled by a graphene/gold bilayer structure. *Commun. Mater.* **2022**, *3*, 56.
[30] Masyukov, M.; Vozianova, A.; Grebenchukov, A.; Gubaidullina, K.; Zaitsev, A.; Khodzitsky, M. Optically tunable terahertz chiral metasurface based on multi-layered graphene. *Sci. Rep.* **2020**, *10*, 3157.
[31] Lee, K.; Son, J.; Park, J.; Kang, B.; Jeon, W.; Rotermund, F.; Min, B. Linear frequency conversion via sudden merging of meta-atoms in time-variant metasurfaces. *Nat. Photonics* **2018**, *12*, 765–773.
[32] Hlaing, M. Z.; Karthikeyan, V.; Wu, W.; Chen, B. J.; Ng, A. K.; Chan, C. H.; De Souza, M. M.; Roy, V. A. L. 3D microstructured frequency selective surface based on carbonized polyimide films for terahertz applications. *Adv. Opt. Mater.* **2022**, *10*, 2102178.
[33] Zhao, X. G.; Wang, Y.; Schalch, J.; Duan, G. W.; Cremin, K.; Zhang, J. D.; Chen, C. X.; Averitt, R. D.; Zhang, X. Optically modulated ultra-broadband all-silicon metamaterial terahertz absorbers. *ACS Photonics* **2019**, *6*, 830–837.
[34] Yun, T.; Kim, H.; Iqbal, A.; Cho, Y. S.; Lee, G. S.; Kim, M. K.; Kim, S. J.; Kim, D.; Gogotsi, Y.; Kim, S. O. et al. Electromagnetic shielding of monolayer MXene assemblies. *Adv. Mater.* **2020**, *32*, 1906769.
[35] Huang, J. H.; Yang, S. D.; Tang, X.; Yang, L. L.; Chen, W. J.; Chen, Z. B.; Li, X. M.; Zeng, Z. P.; Tang, Z. K.; Gui, X. C. Flexible, transparent, and wafer-scale artificial synapse array based on $TiO_x/Ti_3C_2T_x$ film for neuromorphic computing. *Adv. Mater.* **2023**, *35*, 2303737.
[36] Yang, R. L.; Gui, X. C.; Yao, L.; Hu, Q. M.; Yang, L. L.; Zhang, H.; Yao, Y. T.; Mei, H.; Tang, Z. K. Ultrathin, lightweight, and flexible CNT buckypaper enhanced using MXenes for electromagnetic interference shielding. *Nano-Micro Lett.* **2021**, *13*, 66.
[37] Liu, P.; Shi, S. Q.; Ni, Y. X.; Xu, K.; Gao, Q. Q.; Hao, Z. L.; Tian, Z. X.; Xiao, W.; Xu, G. J.; Liu, F. H. Direct ink writing printed flexible double-layer staggered woodpile structure for multi-band compatible absorption of gigahertz and terahertz waves. *Chem. Eng. J.* **2023**, *478*, 147474.
[38] Li, Y. K.; Song, Z. H.; Lin, S. J.; Zhang, L. H.; Jiang, M. Z.; Zeng, L. Z.; Hu, F. R. $Ti_3C_2T_x$ MXene polyester fiber mesh composite as broadband terahertz absorber. *Adv. Mater. Technol.* **2024**, *9*, 2301557.
[39] Luo, M.; Guo, J. C.; Shui, W. C.; Tan, Y.; Huang, H. M.; Yang, Q. H.; Zhang, H. W.; Deng, X.; Wen, Q. Y. $Ti_3C_2T_x$ MXene-based superhydrophobic broadband terahertz absorber with large pore-size foam architecture. *Adv. Mater. Interfaces* **2023**, *10*, 2201767.
[40] Guo, Y. B.; Bai, Y.; Lu, Y. X. Flexible CNT-MXene-CNT film with low surface conductance for high- and low-power electromagnetic absorption protection. *ACS Appl. Electron. Mater.* **2023**, *5*, 6859–6873.
[41] Pai, A. R.; Lu, Y. Z.; Joseph, S.; Santhosh, N. M.; Degl'Innocenti, R.; Lin, H.; Letizia, R.; Paoloni, C.; Thomas, S. Ultra-broadband shielding of cellulose nanofiber commingled biocarbon functional constructs: A paradigm shift towards sustainable terahertz absorbers. *Chem. Eng. J.* **2023**, *467*, 143213.
[42] Ji, J. W.; Wang, Y. L.; Zhao, W.; Wang, G. Laser-induced graphene/TiCN on a polyimide/MXene film as interference shielding materials for terahertz electromagnetic waves. *ACS Appl. Nano Mater.* **2023**, *6*, 23401–23409.
[43] Li, Y.; Xiong, C.; Huang, H.; Peng, X. D.; Mei, D. Q.; Li, M.; Liu, G. Z.; Wu, M. C.; Zhao, T. S.; Huang, B. L. 2D $Ti_3C_2T_x$ MXenes: Visible black but infrared white materials. *Adv. Mater.* **2021**, *33*, 2103054.
[44] Liu, Z. M.; Zhang, S. F.; He, B.; Wang, S. J.; Kong, F. G. Temperature-responsive hydroxypropyl methylcellulose-N-isopropylacrylamide aerogels for drug delivery systems. *Cellulose* **2020**, *27*, 9493–9504.